

An Electro-Photonic System for Accelerating Deep Neural Networks

Cansu Demirkiran*† Furkan Eris* Gongyu Wang† Jonathan Elmhurst† Nick Moore†
 Nicholas C. Harris† Ayon Basumallik† Vijay Janapa Reddi‡ Ajay Joshi* Darius Bunandar†

*Boston University †Lightmatter ‡Harvard University

{cansu, fe, joshi}@bu.edu, {gongyu, jon, nmoore, nick, ayon, darius}@lightmatter.co, vj@eecs.harvard.edu

Abstract—The number of parameters in deep neural networks (DNNs) is scaling at about $5\times$ the rate of Moore’s Law. To sustain the pace of growth of the DNNs, new technologies and computing architectures are needed. Photonic computing systems are promising avenues, since they can perform the dominant general matrix-matrix multiplication (GEMM) operations in DNNs at a higher throughput than their electrical counterpart. However, purely photonic systems face several challenges including a lack of photonic memory, the need for conversion circuits, and the accumulation of noise. In this paper, we propose a hybrid electro-photonic system realizing the best of both worlds to accelerate DNNs. In contrast to prior work in photonic and electronic accelerators, we adopt a system-level perspective. Our electro-photonic system includes an electronic host processor and DRAM, and a custom electro-photonic hardware accelerator called ADEPT. The fused hardware accelerator leverages a photonic computing unit for performing highly-efficient GEMM operations and a digital electronic ASIC for storage and for performing non-GEMM operations. We also identify architectural optimization opportunities for improving the overall ADEPT’s efficiency. We evaluate ADEPT using three state-of-the-art neural networks—ResNet-50, BERT-large, and RNN-T—to show its general applicability in accelerating today’s DNNs. A head-to-head comparison of ADEPT with systolic array architectures shows that ADEPT can provide, on average, $7.19\times$ higher inference throughput per watt.

I. INTRODUCTION

Deep neural networks (DNNs) are commonly used in a range of applications including image and video processing [37], [51], diagnostic medical imaging [69], speech recognition [38], [92], and conversational AI [26]. DNNs can perform impressive human-like tasks enabled by rapid growth in DNN parameter counts. For example, the full version of the Open-AI’s language processing model GPT-1 [62] and GPT-2 [63] have 117 million and 1.5 billion parameters, respectively. The recent GPT-3 model [13] has 175 billion parameters and requires 3.14×10^{23} operations to evaluate a single data. Open-AI’s study shows that from AlexNet (2012) to AlphaGo Zero (2018), the computation requirement has increased $300,000\times$. This trend is projected to continue as the community develops newer DNN models [5].

To support the ever-growing compute requirements of DNNs, numerous highly parallelized computing solutions including massively-threaded graphics processing units (GPUs) [21]–[23], [25], [43], field-programmable gate arrays (FPGAs) [29], [42], [73], [97], and specialized application-

specific integrated circuits (ASICs) [16], [17], [19], [27], [28] have been developed. Broadly speaking, DNN algorithms are centered around the general matrix-matrix multiplication (GEMM) operations that account for more than 90% of the total number of floating-point operations within the network [20]. Therefore, accelerating these compute-intensive GEMM operations can have a significant impact on the overall throughput of the DNNs. CPUs and GPUs use temporal architectures, where single instruction multiple data (SIMD) and single instruction multiple threads (SIMT) are used to parallelize the execution of multiply-accumulate (MAC) operations, and, in turn, accelerate GEMM operations used in DNN inference and training [96]. Spatial architectures including systolic arrays (e.g., Eyeriss [18], Google’s TPU [46], SCNN [59] and NeuFlow [28]) that exploit data-reuse and parallel MAC operations are also used to accelerate GEMM in DNNs. Although several of these solutions provide significant architectural and performance benefits for DNN execution, they are based on CMOS transistors—devices that no longer scale in area or energy consumption according to Moore’s Law and Dennard Scaling.

Here, we explore the use of photonic computing systems for meeting the computational demands of DNNs. The idea of computing with light is not new and has been explored since the 1960s [67]. Replacing traditional CMOS-based transistors with optical transistors is an appealing idea because of the opportunity for obtaining high throughput and high energy efficiency. As a result, free-space optical computers have remained a major research interest over many decades [10], [11], [15], [40]. However, these computers have not been widely adopted due to challenges associated with optical alignment, precision control over the phase and amplitude of the light field, and the component counts required to compete with state-of-the-art digital electronics.

The problem of control and stabilization of many photonic components was largely solved with the advent of integrated photonics. One particular flavor of integrated photonics—silicon photonics—has seen widespread integration in commercial CMOS foundries alongside CMOS transistors on 300-mm wafers [31]. Limitations around photonic information storage and weak photon-photon nonlinearities make it difficult—if not impossible—to design a practical general-purpose optical computing system. Recent works have turned

their focus towards specialized photonic computing units for accelerating DNNs [8], [60], [74], [75], [79], [80], [80], [88], [90]. These efforts leverage highly parallel and efficient linear transformations enabled by photonics.

A key shortcoming of prior works is the lack of a complete end-to-end system-level solution. Reported results [14], [30], [95] have been focused on standalone accelerators performing GEMM and convolution operations [8], [53], [79], [80] on simple neural networks and datasets (e.g., MNIST [48] or Fashion-MNIST [93]). The narrow scope of previous work has lead to unrealistic conclusions and skepticism about the technology.

In this work, ① we introduce a complete electronic-photonic system that combines an electronic host processor and DRAM alongside an electronic-photonic accelerator (called ADEPT). ADEPT consists of a photonic tensor core (a ‘photo-core’) for GEMM, a custom electrical digital ASIC for non-GEMM operations, and large electrical SRAM arrays for storing weight and activation data; ② We introduce architectural optimizations for pipelining GEMM and non-GEMM operations, and for scheduling next-batch DRAM transfers enabling large batch sizes without DRAM spilling; ③ Unlike prior works on photonic accelerators that focused on CNNs and smaller datasets, we use three state-of-the-art neural networks from the MLCommons datacenter inference benchmarks [66] that represent a wide range of operations: ResNet-50 [37] for image classification on the ImageNet dataset [70], BERT-large [26] for natural language processing on the SQuAD v1.1 [64] question answering dataset, and RNN-T [38] as an LSTM-based speech recognition network on the LibriSpeech [58] speech audio dataset; and ④ We perform a head-to-head comparison of ADEPT with electronic systolic arrays and evaluate the full system using metrics including throughput (in inferences per second or IPS), power efficiency (in IPS/W), and power-area efficiency (in IPS/W-mm²). Our analysis shows that, compared to systolic arrays, ADEPT provides **6.35×**, **4.27×** and **10.96×** better power efficiency, **5.85×**, **3.92×** and **10.08×** times better power-area efficiency for the full system for ResNet-50, BERT-large and RNN-T networks, respectively. Broadly, we show that while using photonics technology for computing is promising, claims of tera-inferences per second are not realistic when considering the system as a whole.

II. COMPUTING WITH PHOTONIC DEVICES

A. General Matrix Multiplication (GEMM) Operations

Photonic computing can be used to efficiently perform specialized operations such as matrix vector multiplication. Mach-Zehnder Interferometers (MZIs), a configurable photonic device that controls the interference of two light beams by adjusting the relative phase shift between the beams can be used as a photonic computing unit cell. A simple MZI consists of two directional couplers (DCs) and a differential phase-shift

in between as shown in Figure 1. The transfer function of an MZI can be represented by a 2x2 orthogonal matrix:

$$U(2) = \begin{bmatrix} \sin \phi & \cos \phi \\ \cos \phi & -\sin \phi \end{bmatrix}, \quad (1)$$

where ϕ is the phase difference between the two internal arms of the MZI. In silicon photonics, the phase difference can be provided by delaying light in one arm using multiple mechanisms, including the thermo-optic effect (~ 100 s kHz bandwidth) [36], mechanical effect (\geq MHz bandwidth) [3], [61], and electric-field induced electro-optic effect (\geq GHz bandwidth) [84].

MZIs are typically larger (with a dimension of ~ 100 μ m) than a photonic microring resonator (with a dimension of ~ 10 μ m)—a popular device analyzed in previous studies of photonic deep learning accelerators [8], [79], [80], [83]). Microring resonators, commonly used as sensitive environmental sensors, require ultra-high precision active stabilization for operation (better than the bit precision required by the computation), limiting their practical applicability in photonic computing. The operation of an MZI is sensitive only to the relative phase difference between its two arms (and not the global phase). A single MZI has been shown to achieve an extremely high extinction ratio (ER)¹ of beyond 60 dB [89], whereas the ER of microrings is determined by how closely critical coupling can be achieved which can be limited by their thermal stability [12]. State-of-the-art demonstrations of a single microring resonator have their measured ER at < 25 dB [76].

A larger $U(m)$ orthogonal matrix (with $m > 2$) can be composed by tiling $m(m-1)/2$ MZIs [24], [65]. Any general $m \times m$ matrix M can then be physically realized through its singular value decomposition (SVD) [35], [54], i.e., $M = U\Sigma V^T$, where U and V^T are $m \times m$ orthogonal matrices; Σ is a diagonal matrix of (non-negative) singular values. Figure 1 shows two orthogonal circuits (V^T, U) connected by a column of single MZIs that are used as variable attenuators implementing Σ . A matrix-vector multiplication (MVM) between a matrix M and a vector v_{in} can then be achieved by (1) programming the matrix M in the array of MZIs; (2) encoding the vector v_{out} in the amplitude and phase (0 or π for sign) of the optical signals entering the array; and (3) obtaining the resulting vector $v_{out} = M \cdot v_{in}$ at the output of the array. When the vector v_{in} is inserted at gigahertz rate, a 100×100 array enables us to perform linear operations at 10 Tera Operations per Second (TOPS). A GEMM operation between two matrices can be achieved by encoding one matrix in the array and by sending the other matrix through the array, one vector at a time.

B. Non-linear Operations

Any non-linear operation (e.g., nonlinear activation functions or conditional if-else statements) on the optical electromagnetic (EM) waves requires the use of nonlinear optical media [44], [55]. Nonlinear optical activation function

¹The ER is a measure of how precise the light signals can be modulated by the photonic device.

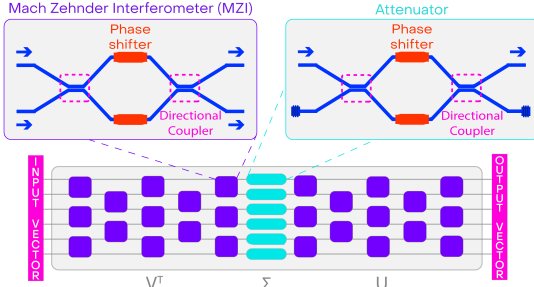


Fig. 1: Programming a matrix by singular value decomposition using Mach-Zehnder Interferometers and Attenuators.

has previously been demonstrated using laser-cooled atoms which absorb light up to some saturation intensity (higher intensity light is absorbed more) [98]. Saturable absorbers, where the amount of light absorbed decreases with increasing light intensity, have also been proposed as optical nonlinear activations [9], [75]. However, the practical implementation of these nonlinear optical activations remains challenging, especially since (1) they have not been miniaturized, and (2) repeated usage of the nonlinear activation function will decay the signal quickly. If the transmissivity of the nonlinear activation function is $\sim \eta$ (≤ 1), then an optical signal with power P_0 propagating through an L -layer network with this activation function will decay exponentially to $\sim \eta^L P_0$.

Semiconductor optical amplifiers (SOAs) made out of III-V materials, e.g., InP and InGaAs, can amplify the optical signal to combat the loss described above [68]. While in principle the optical DNN accelerator can be built in the III-V platform itself [77], [78], researchers still prefer to use silicon photonics as it has been monolithically integrated with the CMOS-based transistors [31] needed for controlling the photonic components. Packaging the III-V module with a silicon photonics module poses a challenge to its feasibility. Even when a practical packaging solution is available, the amount of power needed to maintain the optical signal throughout the entire evaluation will increase exponentially with the number of neural network layers. Hence, we argue that non-linear operations should not be performed in the photonic domain.

C. Numerical Precision

The error accumulation and preservation of the numerical precision have been the main challenges in analog computing. Similarly, in photonic computing, it should be taken into account that the numerical precision of the output vector v_{out} observed at the output of the MZI array is limited by how well one can encode the input vector v_{in} and the matrix M . In this section, we relate the bit precisions of the input vector and the weight matrix with the bit precision of the output vector mathematically.

The error of the weight matrix M can be calculated by considering that all classical photonic operations (in our case, these are the transformations afforded by U , Σ , and V^T) are unitary/orthogonal transformations. We are then primarily interested in obtaining the magnitude of the perturbation

ΔM , quantified by the normalized Frobenius norm $\|\Delta X\|^2 = \sum_{ij} |\Delta X_{ij}|^2 / m$, where X is a placeholder for U , Σ , or V^T .

Two (realistic) limitations provide the major contribution to the perturbation of each transformation. The first is the phase encoding error. We consider the error of the phase encoding to be quantified as $\varepsilon_\phi \leq 2^{-b_w}$, where b_w is the bit precision of the weight digital-to-analog converters (DAC). The matrix perturbation induced by a single-phase setting error is: $\|\Delta X\|^2 \approx \varepsilon_\phi^2 / m$ [7]. The second important source of transformation error is the component error. Given that the matrix is composed of MZIs, which only use 50:50 DCs, we only need to consider the DC splitting error. The matrix perturbation induced by a single DC error ε_{DC} (typically due to fabrication imperfections) is $\|\Delta X\|^2 \approx 2\varepsilon_{\text{DC}}^2 / m$ [7].

Realistically, fabrication imperfections are often correlated: neighboring DCs will be perturbed in a similar manner. However, correlation can add significant complexity, obfuscating mathematical insight. Monte-Carlo simulation tools should be used to quantify the errors when correlations exist. For the remainder of the calculation, we assume an uncorrelated error model for both the encoding and the component errors.

Under the uncorrelated error model, the error terms can be added in quadrature. In each MZI, there are two DCs and a single-phase shifter. In the Σ matrix, there are only m parallel MZIs, thus $\langle \|\Delta \Sigma\|^2 \rangle = \varepsilon_\phi^2 + 4\varepsilon_{\text{DC}}^2$. In the matrices U and V^T , there are $m(m-1)/2$ MZIs. The depth of the photonic circuits in M grow as $O(m)$, and component (uncorrelated) errors cascade as light propagates down the mesh. A naïve programming of the phases will result in a U or V^T matrix error that grows as $\propto m\varepsilon^2$ [24], [65].

More sophisticated error-corrected programming strategies [7], [33], [34], however, can achieve a better scaling with respect to the component errors, such that

$$\langle \|\Delta U\|^2 \rangle = \langle \|\Delta V^T\|^2 \rangle = \frac{m(m-1)}{2} \left[\frac{\varepsilon_\phi^2}{m} + 2 \frac{2\varepsilon_{\text{DC}}^4}{3m} (m+1) \right], \quad (2)$$

where the first term in the square bracket is the contribution due to phase encoding error and the second is due to component error. The corrected programming strategy effectively allows for a squaring of the component errors that is advantageous when $\varepsilon_{\text{DC}} \leq m^{-1/2}$. Finally, the error for the overall matrix M can therefore be defined as:

$$\Delta M = \sqrt{\langle \|\Delta U\|^2 \rangle + \langle \|\Delta \Sigma\|^2 \rangle + \langle \|\Delta V^T\|^2 \rangle}. \quad (3)$$

The quantity above can be understood as the average relative error of each element of matrix M . The precision of the output vector v_{out} can now be quantified by adding the input vector and the matrix errors in quadrature: $\Delta v_{\text{out}} = \sqrt{\Delta v_{\text{in}}^2 + \Delta M^2}$. The error of the input vector encoding Δv_{in} can be quantified as, $\Delta v_{\text{in}} \leq 2^{-b_{\text{in}}}$, where b_{in} is the bit precision of the input DACs. The output vector will be captured by analog-to-digital converters (ADCs) with bit precision of b_{out} . In order for the output vector error to be dominated by the bit precision of the ADCs, we require $\Delta v_{\text{out}} \leq 2^{-b_{\text{out}}}$. Assuming a reasonable DC

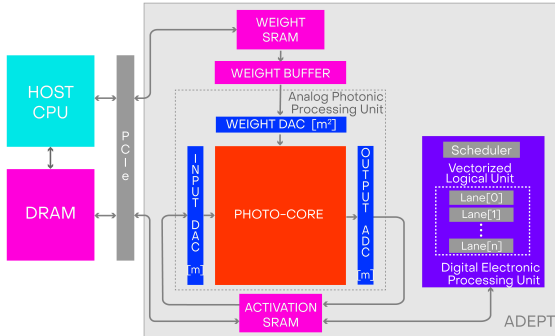


Fig. 2: Full system consisting of Host CPU, DRAM and ADEPT.

splitting error of $< 0.1\%$ (this quantity should be measured in the fabricated silicon photonic wafer), we can determine that the precision of the output vector can be maintained up to ~ 8 bits for matrices up to size 256×256 if the input and the weight DAC bit precisions are 10 and 12 bits, respectively. We shall make use of these bit precisions in designing our hybrid electro-photonic accelerator.

The discussion above provides important intuition as to how errors compound in an analog photonic computer. The analysis effectively relates the signal-to-noise ratio (SNR) of the input and the weight DACs with the SNR of the output ADC. Note that the input and the weight data to be encoded in the photonic GEMM device can have fewer than b_{in} and b_w bits, respectively—they just have to be encoded using DACs with SNRs commensurate to the prescribed bit precisions.

III. ELECTRO-PHOTONIC SYSTEM DESIGN

In this section, we provide an overview of the electro-photonics system in Section III-A. In addition, we provide microarchitecture details of ADEPT’s analog photonic computing unit, digital electronic processing unit and memory units in Sections III-B, III-C and III-D, respectively. The electro-photonics system is custom-designed for DNN inference operation. We leave the customization for training of DNNs as part of future work.

A. Full System Architecture

Focusing on linear operations alone in the photonics domain will not be sufficient to evaluate the use of photonics for end-to-end DNN acceleration. Therefore, in this work we propose—for the first time—a full electro-photonics system architecture consisting of a host CPU, DRAM and ADEPT, which comprises an analog photo-core (size of $m \times m$), memory units, DACs, ADCs, and a digital electronic ASIC (see Figure 2). ADEPT is connected to the host CPU and DRAM through a PCI Express (PCI-e) bus. ADEPT uses an analog photo-core for performing linear GEMM operations and a digital electronic ASIC for performing non-GEMM operations. ADEPT also uses an SRAM array for input and output activations, and a separate SRAM array for storing the weights. Data from the SRAM are encoded using DACs and then input to the analog photo-core. When the calculations are

complete, ADCs are used to convert the results into digital domain and the data are then written back to the SRAM. We use a weight buffer as a staging area. We overlap GEMM operation (using the currently programmed weight matrix) with transferring the weight data from weight SRAM to weight buffer for the next GEMM operation. The weights from the weight buffer can then be rapidly programmed into the MZI array without incurring the large data transfer latency from the weight SRAM.

B. Analog Photonic Computing Unit

The photonic computing unit in ADEPT is an analog unit designed to perform MVM operations that can eventually be composed into a GEMM operation (see Section II-A). The unit consists of the input modulators (Mach-Zehnder Modulators or MZMs), an array of MZIs, photo-detectors, ADCs and DACs. We refer to the unit without ADCs and DACs as the photo-core.

GEMM operations within DNNs typically involve a multiplication between a weight tensor and an input tensor. This multiplication is performed as a series of MVMs in the photo-core. We adopt the weight stationary (WS) approach for performing GEMM, where the weight matrix is programmed into the MZI array and the input vector is encoded in the optical signals. To program the weight matrix into the MZI array, the matrix must be decomposed into two orthogonal matrices and a diagonal matrix of singular values. This SVD operation can be performed offline and the two orthogonal matrices can be loaded into the DRAM before any inference operation. One can also consider an input stationary (IS) approach where the input matrix, instead of the weight matrix, is programmed into the MZI array. However, the current architecture of photo-core prohibits the IS approach because (1) the input matrix of a DNN layer must be computed at runtime and (2) SVD, which has the same computational complexity of a GEMM operation, needs to be performed on the matrix to be programmed into the array. Similarly, output stationary (OS) is not feasible in this architecture because it would require updating the values programmed into MZIs each cycle. In our WS approach, the weight values to be programmed into the MZI array are first transferred from the weight SRAM into the weight buffer while MVM operations can continue in the photo-core. Data from the weight buffer can be programmed into the photo-core at a rate limited by the modulation mechanism of the MZIs—during which, the photo-core is inoperable. This overhead is unavoidable but it is fairly small ~ 10 ns [85]. Digital values corresponding to both weight and input are converted into analog values using the DACs. The input and the weight DACs are 10-bit and 12-bit precise, respectively, which are adequate to guarantee 8-bit precise outputs (see Section II-C).

The output of the MVM operation (both amplitude and sign) is detected using coherent detectors, e.g., homodyne or heterodyne detectors, with the help of a local oscillator. The resulting photocurrent output of the coherent detectors is eventually converted into digital bits, using 8-bit ADCs, that are stored back into the activation SRAM. These values are

passed to the electronic processing units that will perform the non-GEMM operations.

C. Digital Electronic Processing Unit

Although typically more than 90% of the DNN inference operations are GEMM operations, a non-trivial amount of non-GEMM operations must also be performed as part of DNN inference. These operations include element-wise non-linear operations (e.g., ReLU, GELU, sigmoid, and tanh); reduction operations (e.g., softmax and max-pool); batch and layer normalizations; and element-wise multiplication and addition (e.g., bias). As discussed in Section II-B, these non-GEMM operations are more effectively performed in the digital domain, using a digital electronic ASIC, instead of the analog domain. Within the digital electronic ASIC, the electronic processing unit is vectorized and the number of lanes in the digital electronic ASIC is equal to the number of optical lanes (channels) in the photo-core. Each lane has a multiplication unit, an addition unit, a division unit, a max unit, a square root unit, and an exponential unit that enable the system to complete the wide variety of non-GEMM operations. These units are implemented as custom digital CMOS circuits. Input vector data for the non-GEMM operations (output of an MVM operation) are read from the activation SRAM, and each element of the vector is operated in an individual vector lane.

To extract the maximum performance from ADEPT, the throughput of the photo-core must be matched with the throughput of the digital electronic ASIC. It is, however, challenging to design a digital ASIC that can operate at high frequencies (e.g., above 2 GHz). Hence, we parallelize and use n logical units for each operation within individual vector lane. Each unit operates at $1/n$ times the clock frequency f_c of the photo-core (each offset by $1/f_c$ to one another) to match the throughput of photo-core.

D. Memory Units

ADEPT utilizes two separate SRAM units: one for input/output activations and one for weights. The SRAM units can transfer data between each other through direct memory access (DMA) and communicate with the host and DRAM through the PCI-e fabric. The two SRAM units are separated because, generally, a dichotomy exists between the activations and the weights, and data transfer between them is not frequent. The activation SRAM is unified in the sense that it is used to store both input and output activations because effectively, the output of one layer is the input of the next layer.

ADEPT also utilizes an additional weight buffer. The weight buffer allows weight data for the next set of GEMM operations to be fetched from the weight SRAM while the photo-core is performing GEMM operations with the current weight values. This pipelining of weight fetching and GEMM operations increases the system's overall utilization and throughput.

IV. EXECUTING DNN ON ADEPT

In this section, we explain the process of executing a given DNN on ADEPT. The compiler (Figure 3) takes a DNN model

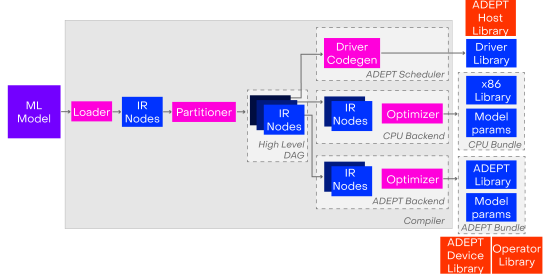


Fig. 3: *Compilation process of a given ML model for ADEPT* as input and compiles it to generate a program specified via a graph on tensor types. It has a cost-model based partitioner that creates a directed acyclic graph (DAG) with 3 sets of nodes: operations to execute on the host CPU (e.g., input pre- and post-processing, etc.); operations to execute on ADEPT (e.g., ML operations such as GEMM, convolutions, non-linear operations, etc.); and a set of driver nodes for moving data between the host and ADEPT. The host CPU operations are optimized to produce a layout that reduces the overall data movement overheads via a CPU back-end in the compiler. The generated code for these three partitions are linked with libraries shown in Figure 3 to produce two executable binaries: one for the host and one for ADEPT. The host executable initiates execution of the DNN. It should be noted that the host CPU performs the compilation only once and then offloads the inference to ADEPT. Pre- and post-processing (e.g., resizing, decoding, etc.) are handled by the host CPU for each input. Effectively, pre-processing, inference, and post-processing for consecutive batches happen in parallel. The different types of operations in DNNs are scheduled by the compilation process onto different units of digital electronic ASIC. These operations are mainly grouped as GEMM and non-GEMM operations.

A. GEMM Operations

The various GEMM operations in a neural network, e.g., in the fully-connected (FC) layer and the 2D convolution layer, are evaluated in the photo-core. While the multiplications in the FC layer can be mapped directly to the photo-core, to perform 2D convolution with the photo-core, we use the image-to-column (im2col) pre/post-processing method that casts the convolution between two 4D tensors into a GEMM between two 2D matrices [6].

The layer shapes vary for different input and weight matrices in DNNs but the photo-core has a fixed $(m \times m)$ tile size. Therefore, to multiply matrices with sizes bigger than $m \times m$, the matrices have to be divided into blocks or tiles (see Figure 4). Each tile of $m \times m$ submatrix can be loaded into the photo-core one-by-one. If any of the dimensions of the large matrix is not an integer multiple of m , then the matrix is padded with zeros to satisfy this condition.

To start the matrix-matrix multiplication process, the first weight submatrix tile is loaded into the photo-core. This submatrix is maintained in the MZI array while all input vectors that need to be multiplied with this particular tile are fed into the photo-core vector-by-vector. Therefore, the input

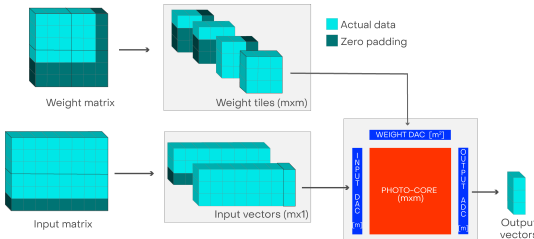


Fig. 4: Example of a GEMM operation using an $m \times m$ photo-core. The weight matrix is divided into $m \times m$ tiles. One MVM is completed between an input vector and the corresponding weight tile every clock cycle, and one partial output vector is obtained.

matrix is divided into $m \times 1$ vectors. Once all multiplications involving the current submatrix tile are completed, the next tile is programmed into the MZI array, and that tile is multiplied with the corresponding input vectors. Partial results are accumulated digitally to construct the final output matrix.

B. Non-GEMM Operations

A number of different non-GEMM operations are required in DNNs. These operations can use only one unit in the digital electronic processing unit (e.g., ReLU) or can be constructed by using different units (e.g., softmax). Element-wise operations can be processed independently in each vector lane and can be distributed without consideration between the different lanes. Kernel-wise independent operations, such as max pooling and average pooling, are distributed across the lanes in the digital electronic ASIC in an output-stationary manner such that all operations can be completed within a single vector lane without any communication between lanes. Similarly, channel-wise dependent operations, such as softmax, require all data from a single channel to be sent to one vector lane and computed within that single vector lane. Batch normalization layer is folded into the filter of the convolutional layer preceding it [45]. In contrast, layer normalization requires calculating mean and variance at runtime and handled by the digital electronic ASIC. In some cases, the same data may be needed for different operations, and thus data duplication may be necessary. The outputs of electronic processing unit are written back to the activation SRAM—to be used in the next layer of the neural network.

C. Parallelism within ADEPT

ADEPT can be scaled up to include multiple photo-cores. We offer two parallelization strategies for distributing the workload among multiple photo-cores: data parallelism and tile parallelism. Data parallelism aims to accelerate MVMs by copying the same weights to all photo-cores. Each photo-core performs the same operations on different inputs in a batch. Tile parallelism is a fine granularity model parallelism that distributes different tiles of a weight matrix in one layer across multiple photo-cores. In contrast to data parallelism, all inputs in one batch are sent to all photo-cores. Digital electronic ASIC can also use Wavelength Division Multiplexing (WDM)-based parallelism. WDM uses multiple wavelengths for encod-

ing different input vectors at once similar to data parallelism. The scheme requires multiplexing and demultiplexing circuits that can be constructed from microring resonators [12] or cascaded unbalanced MZIs [94]. WDM parallelism is similar to data parallelism, but the same MZI array and weight DACs can be used by all inputs encoded in the wavelengths.

V. ADEPT DESIGN OPTIMIZATIONS

In this section, we introduce optimizations for minimizing overhead of non-GEMM operations and DRAM transfers in ADEPT.

A. Pipelining GEMM and non-GEMM Operations

GEMM and non-GEMM operations in ADEPT can be pipelined. Specifically, once an *output vector* (after accumulating the partial output results) of a GEMM operation has been generated, that output vector can be immediately sent to the digital electronic ASIC for non-linear operations. Therefore, non-GEMM operations can begin without the need to wait for the whole GEMM layer to be completed (for example, other MVM operations for the GEMM layer can still continue in the photo-core).

Additionally, more than one non-GEMM layer can follow each other, or one non-GEMM layer may need to use more than a single logical unit. ADEPT can be further optimized by pipelining these non-GEMM operations. For example, the softmax layer uses the exponential unit, the max unit, and the multiplication unit. While one element is using the exponential unit, the previous output of the exponential unit can use the max unit. As a result, as long as the data dependency is preserved, different non-GEMM operations or different steps using different logical units in the digital electronic ASIC within a non-GEMM operation can be parallelized and pipelined.

B. Maximizing the Batch Size

ADEPT's throughput is limited by the rate at which data are input into the photo-core. While the latency and bandwidth of activation and weight SRAM arrays can be designed to match the throughput of the photo-core, the sizes of these arrays are limited. If the activations and weights do not fit within these SRAM arrays, frequent DRAM accesses would be necessary. These DRAM accesses are slower compared to SRAM accesses and can easily bottleneck the system performance.

To avoid being bottlenecked by DRAM latency during runtime, we may want to limit the batch size for a given neural network. On the other hand, larger batch sizes provide a better throughput. We, therefore, introduce an optimized buffering method which maximizes the batch size stored in the activation SRAM without ever spilling back to the DRAM during runtime. This method takes advantage of the empty space in the SRAM during inference and loads the inputs of the next batch from DRAM efficiently.

We describe this optimized buffering method as a convex optimization problem. First, let us express the memory usage of a neural network as a function of time. Let

$\vec{x}_c = [x_c(t_0), x_c(t_1), \dots, x_c(t_{\max})]$ be a vector representing the activation SRAM array usage while evaluating the current batch of activations over time. We have $t_{i+1} = t_i + \Delta t$, and Δt is some time interval chosen to ensure the optimization problem is tractable for the host CPU. Here t_0 refers to the time when inference for the current batch starts, and t_{\max} refers to the time when it finishes. Similarly, $\vec{x}_{\text{pcie}} = [x_{\text{pcie}}(t_0), x_{\text{pcie}}(t_1), \dots, x_{\text{pcie}}(t_{\max})]$ is a vector representing the activation SRAM usage of the data being transferred from DRAM into SRAM over time.

Next, we can calculate the difference $\Delta \vec{x}_{\text{pcie}} = [\Delta x_{\text{pcie}}(t_0), \Delta x_{\text{pcie}}(t_1), \dots, \Delta x_{\text{pcie}}(t_{\max})]$ where $\Delta x_{\text{pcie}}(t_i) = x_{\text{pcie}}(t_i) - x_{\text{pcie}}(t_{i-1})$. For a given \vec{x}_c , an optimal \vec{x}_{pcie} data transfer schedule can be obtained by solving the following linear program:

$$\begin{aligned} \text{Maximize:} \quad & \sum_{t=t_0}^{t_{\max}} x_{\text{pcie}}(t) \\ \text{Subject to:} \quad & 0 \leq x_c(t) + x_{\text{pcie}}(t) \leq x_{\max}, \\ & x_{\text{pcie}} \geq 0, \\ & x_{\text{pcie}}(t_{-1}) = 0, \\ & x_{\text{pcie}}(t_{\max}) = x_{\text{input}}, \\ & 0 \leq \Delta x_{\text{pcie}}(t) \leq \text{Max. PCI-e bandwidth} \end{aligned}$$

The constraints in the optimization problem can be understood as (1) the total SRAM usage will be less than the given SRAM size (x_{\max}) (2) will not be negative at any time and (3) will start from zero, (4) the total amount of data transferred will be equal to the input size of the next batch, (5) the data transfer rate must be slower than the maximum PCI-e bandwidth. The objective function is to maximize the area under the curve of memory usage of the transferred data for the next batch. Maximizing this area guarantees transferring the data *as soon as possible* under the constraint of a maximum PCI-e bandwidth.

If the program fails to return a schedule $x_{\text{pcie}}(t)$ that meets the specified constraints for a given batch size and maximum PCI-e bandwidth, a smaller batch size or a larger bandwidth (if it is available on the hardware) should be chosen. We use the above linear program to find the *largest* batch size which ensures that the memory usage from storing (input and output) activations of the current batch and the input of the next batch never exceeds the SRAM size. As such, we ensure that all DRAM data transfer for the next batch of inputs can happen simultaneously with the inference of the current batch. The optimized schedule is computed only once by the compiler before runtime.

VI. EVALUATION METHODOLOGY

We choose systolic array structures as the comparison point for our work because of the similarity in between the dataflows of ADEPT and systolic arrays, as well as the common usage of systolic arrays for accelerating DNN [18], [28], [46], [59]. We provide power, performance and area comparison for both standalone GEMM accelerators and for the full system.

Architecture-level Analysis: We used SCALE-Sim [71] to model ADEPT and electronic systolic arrays. SCALE-Sim is a simulator that takes as inputs, the systolic array configuration

(i.e., array size and dataflow type) and the neural network configuration (i.e., layer sizes and batch size), and calculates the number of cycles needed to execute the neural network. The simulator also generates traces for SRAM and DRAM reads/writes.

We modified SCALE-Sim to model the performance of the photo-core in ADEPT. In addition, we unified the separate input and output SRAMs in SCALE-Sim into a single activation SRAM (Fig. 2). SCALE-Sim enables us to simulate our dataflow and directly compare the performance of the photo-core with that of systolic arrays. However, SCALE-Sim only models the GEMM operations. Thus, we designed the parts of digital electronic ASIC that executes the non-GEMM operations using SystemVerilog RTL. We also incorporate the optimizations described in Section V in our evaluation. The optimizations—operation pipelining and DRAM transfer optimization—are handled by the compiler in a full-system. We evaluate the effects of these optimizations using analytical models. For our evaluation, we choose three DNNs: ResNet-50 [37], BERT-large [26], and RNN-T [38]. These three state-of-the-art networks—all part of the MLCommons inference data-center benchmarks [66] in the *offline* scenario—represent the diversity in layer types, sizes, and shapes that we observe in DNNs.

Circuit/Device-level Analysis: For a realistic power, performance, and area comparison, we designed the digital electronic ASIC units and systolic arrays at RTL level and then synthesized them using Cadence Genus [1] with a standard cell library designed in the GF22FDX technology node [2]. The SRAM arrays required by both digital electronic ASIC and electronic systolic arrays were generated using an SRAM compiler for GF22FDX. The SRAM arrays were designed such that they have a single-cycle read/write access.

The photo-core is powered by a laser. We can calculate the required laser power per channel P analytically by considering (1) the laser wall-plug efficiency, (2) the losses of the various optical devices, and (3) the SNR needed for an 8-bit output, as follows:

$$P = \frac{(\kappa \text{ SNR}_{\text{shot}})^2 \cdot (q \Delta f / 4)}{\eta_{\text{det}} \cdot \eta_{\text{array}} \cdot \eta_{\text{mod}} \cdot \eta_{\text{cpl}} \cdot \eta_{\text{laser}}}, \quad (4)$$

where SNR_{shot} is the SNR assuming shot noise only and κ (assumed to be ≈ 3) accounts for noise contributions (e.g., thermal noise and transistor noise) other than the shot noise. The overall $\text{SNR} = \kappa \text{ SNR}_{\text{shot}} = 2^{b_{\text{out}}}$ with b_{out} being the bit precision of the output ADC. Here, q is the elementary charge, and Δf is the bandwidth of the coherent detector (related to the clock frequency). The η 's account for the transmissivity from the laser to the detectors. η_{mod} is the transmissivity of the modulator (≈ 1.2 dB loss [4]), η_{array} is the transmissivity of the MZI array (≈ 0.04 dB loss per MZI [61], [87] and each signal passes through $2m + 1$ MZIs), η_{cpl} is the fiber laser-to-chip coupling efficiency (≈ 2 dB loss), η_{det} is the efficiency of the photodetectors ($\approx 80\%$ [50]), and η_{laser} is the wall-plug efficiency of the laser ($\approx 20\%$ [57]).

The necessary bit precisions for the inputs and the weights are 10 bits and 12 bits, respectively, to guarantee the 8-bit-precise outputs read by the ADCs (See Section II-C). However, we use 14-bit DACs [41] with a 10 GS/s sampling rate and 177 mW power consumption designed with 28 nm CMOS technology for both inputs and weights to keep the technology node as similar as possible to the RTL designs in GF22FDX. A widely accepted figure of merit (FoM) for the performance of DACs is $\text{FoM} = 2^B \cdot f_s|_{6(B-1)} / P_{\text{DAC}}$. Here, B is the bit precision of the DAC, $f_s|_{6(B-1)}$ is the output signal frequency where the spurious free dynamic range has dropped with 6 dB ($= 1$ bit) in comparison with the expected results ($\approx 6B$), and P_{DAC} is the power consumption of the whole DAC [49], [86]. In essence, the power consumption of a DAC—with the same FoM—is proportional to 2^B . Therefore, a 12-bit DAC (for the weights) with the same FoM will consume $2^2 = 4$ times less power than a 14-bit DAC. Similarly, a 10-bit DAC (for the inputs) with the same FoM will consume $2^4 = 16$ times less power than a 14-bit DAC. The 10-bit input and 12-bit weight DACs will then consume 11.06 mW and 44.25 mW, respectively. The output ADCs within ADEPT have a 5 GS/s sampling rate and consume 29 mW each [32]. The electronic-to-optical (E-O) and optical-to-electronic (O-E) conversion power is based on the total energy required to operate the modulator circuitry, which is ~ 20 fJ/bit, and the detector circuitry, which is ~ 297 fJ/bit [81]. The average conversion power is then calculated by dividing the total conversion energy by the total inference time. Similarly, the average DRAM power is calculated by counting the total number of DRAM accesses, tallying the total energy by assuming ~ 20 pJ/bit access [39], and then dividing this energy by the total inference time.

VII. EVALUATION RESULTS

A. Photo-core vs. Electronic Systolic Arrays

We first compare ADEPT’s photo-core against electronic systolic arrays in terms of throughput, power, and power efficiency when both arrays are isolated from the system.

1) *Throughput*: We analyze the throughput—in terms of inferences per second (IPS)—for a WS ADEPT and compare it with systolic arrays with different dataflows (input stationary (IS), output stationary (OS), and WS). The analysis is done with the three DNN workloads and includes only GEMM operations. For the comparison, we use a single 128×128 array (the choice of size is justified later in this section) for both the photo-core and the systolic array. We assume both weights and inputs have already been loaded and are available in the SRAM with reads/writes that are fast enough to keep up with the requirements of both arrays. Figure 5(a) shows the comparison between the performance of the photo-core and that of the systolic array operating at 1 GHz clock frequency for different batch sizes. Importantly, the figure compares the performance of the two compute arrays for three different networks—ResNet-50, BERT-large, and RNN-T—separately (one plot per network). In the photo-core, one MVM operation is completed every clock cycle after the weight tile has been

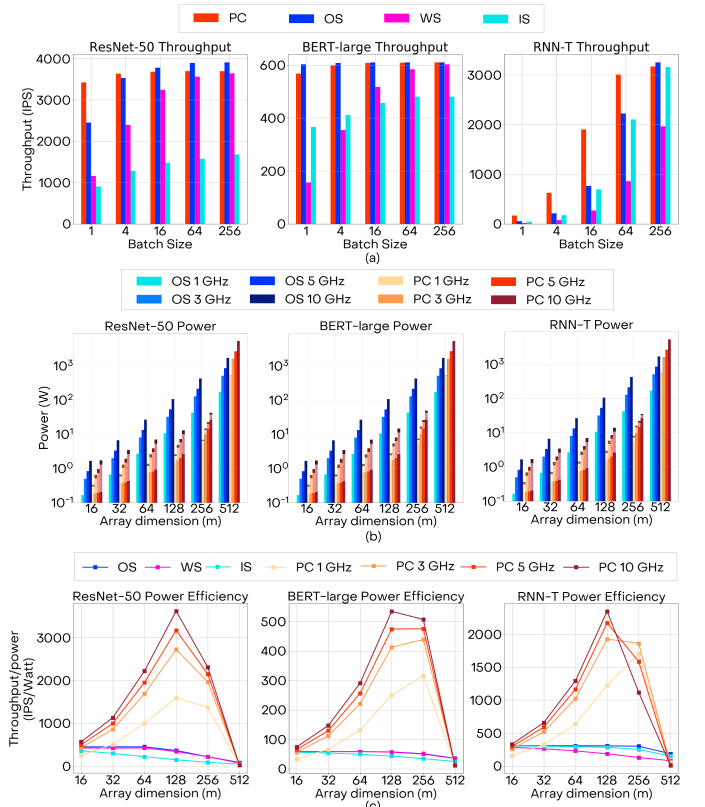


Fig. 5: (a) Throughput vs. batch size of 128×128 photo-core (PC) and systolic arrays with OS, WS, and IS dataflows at 1 GHz clock.

(b) Power consumption of the OS systolic array and the WS photo-core, for different array sizes at 1, 3, 5, and 10 GHz clock. The power consumption of the photo-core is broken down into the power requirements of its laser (solid color), ADCs/DACs (white diagonal pattern) and E-O/O-E conversion (black diagonal pattern).

(c) Power efficiency (in IPS/W) of OS, WS, IS systolic arrays and WS photo-core for different array sizes at 1, 3, 5, and 10 GHz clock.

loaded into the photo-core. In contrast, in a systolic array, it takes m clock cycles to complete a single MVM operation. If the matrices to be encoded are larger than the systolic array size, the matrices are tiled as described in Section IV.

Throughput vs. Dataflow: It is important to understand the different dataflows in systolic arrays. OS dataflow keeps the outputs stationary in the processing elements (PEs) while accumulating the MAC results flowing through the PEs. Since all the outputs (the registers in PEs) start their accumulation from zero, this dataflow does not require any initial latency for loading values into the registers before starting the MAC operations. On the other hand, for WS/IS dataflows, the values in a particular tile of weights/inputs must first be loaded into the registers. One row/column of the weights/inputs are loaded per clock cycle from one side of the systolic array, and the values shift between PEs until all the elements in the tile matrix are loaded. For example, 128 cycles are required to

load a 128×128 weight/input matrix into the 128×128 systolic array with WS/IS dataflows before the MAC operations can begin. We observe from Figure 5(a) that, for systolic arrays, OS performs better in terms of throughput than the other two dataflows due to this initial latency. So, we use OS systolic array for the rest of the analysis.

In contrast, in the photo-core, we do not load the weight values one vector per clock cycle. We can program all the weights of a tile into the MZI array in parallel in a total of 10 ns (See Section III-B). It should be noted that this latency is fixed and independent from the clock frequency. For all networks, the WS photo-core performs better than the WS systolic array. This is due to the use of the weight buffer in the photo-core and the lower latency for loading weight tiles into the MZI array. As the batch size increases, latency for loading the weights in between tiles becomes less important because more time is spent on performing MVM operations in each tile. We can observe that WS systolic array's throughput gets closer to the photo-core's throughput as the batch size increases.

The performance of the different dataflows are dependent on the sizes of input and weight matrices. We observe that the photo-core's WS dataflow is more advantageous when the weight matrices are large and the input matrices are small (e.g., RNN-T with small batch sizes) because each weight tile needs to be loaded only once. In contrast, when the weight matrices are small but the input matrices are large (e.g., ResNet-50 with large batch sizes), the OS systolic array dataflow is more advantageous.

Throughput vs. Batch Size: As the batch size increases, the number of vectors multiplied with the same weight tile increases. Therefore, the photo-core's and the WS systolic array's utilization and throughput increase as well. Among the different networks, we observe that the throughput saturates for ResNet-50 and BERT-large more quickly than RNN-T. The small input matrices in RNN-T means fewer number of vectors are multiplied with the same tile. The utilization and throughput continue to significantly increase until we have larger batch sizes for RNN-T. Broadly, at the same clock frequency, ADEPT's photo-core can provide comparable or better performance (in terms of IPS) than the best-performing systolic array.

Operating Frequency: One way to increase the throughput of any computing device is to increase the clock frequency. We therefore attempt to increase the clock frequency of the photo-core and the systolic arrays (from 1 GHz to 3 GHz, 5 GHz, and 10 GHz). The photo-core which utilizes light, which in turn oscillates at hundreds of terahertz, has a significant bandwidth advantage over the electrical systolic arrays which are constrained by the bandwidth limitations due to parasitic resistance, capacitance, and inductance.

In case of systolic arrays, Cadence Genus with GF22FDX failed to meet the timing requirements for clock frequencies of 3 GHz and above. Therefore, we use parallelism instead to effectively operate the systolic array at higher frequencies. For example, to operate a systolic array at 5 GHz, we use five

1 GHz systolic arrays whose clock cycles are offset by 200 ps to one another. The latency of this parallelized systolic array will still be 1 ns, but its throughput will be synonymous to a single systolic array operating at 5 GHz.

The throughput of the systolic arrays will increase linearly with the clock frequency. The rate of MVM operations in a photo-core also increases linearly with the clock frequency. However, a fixed 10 ns is necessary for programming the MZI array and is independent from the clock frequency. Therefore, the increase in the throughput of the photo-core will be less than linear. As the number of vectors to be multiplied with a weight tile increases, the 10 ns latency can be amortized over many MVM operations, and the increase in throughput gets closer to be linear.

2) Power Consumption: An increase in the operating frequency results in a corresponding increase in power consumption. Figure 5(b) compares the average power consumed by the WS photo-core (laser, ADC/DAC, and E-O/O-E conversion) and the OS systolic array of different sizes. For an $m \times m$ photo-core, we need m DACs for the input vector and m ADCs for the output vector. These input/output DACs/ADCs perform a conversion each cycle. Additionally, we need DACs for programming the $m \times m$ weight matrix, and this can be completed within 10 ns. Within this 10 ns constraint, a single 10 GS/s DAC can be used to perform conversion for 100 weight elements. Therefore, instead of using m^2 DACs, we use $\lceil m^2/\zeta \rceil$ DACs for weights where ζ is equal to 100. Besides, these DACs for programming the weights into the MZIs are not used each cycle. The weights are programmed into the MZI once for each tile, and the DACs are not used until all MVMs for the corresponding tile are finished. As the number of vectors to be multiplied increases (dependent on the size of the input matrix and batch size), the contribution of the weight DACs to the overall power consumption decreases.

For our analysis, we use a batch size of 256 to ensure that the throughput is nearly saturated for all networks. For the systolic arrays, the power consumption increases linearly with the number of PEs ($m \times m$). The power consumption also increases linearly with clock frequency when we use multiple 1 GHz systolic arrays in parallel to achieve a higher operating clock frequency.

For the photo-core, the number of conversions stays the same while the number of DACs/ADCs for input/outputs increases linearly with m . The number of DACs for weights increases quadratically with m . The average power consumption of DACs/ADCs increases because the inference latency drops as the array size increases. In other words, the same number of conversions are performed within a shorter duration of time. Moreover, the laser power increases exponentially with the depth m of the array, due to optical loss. As a result, laser power dominates for larger array sizes. Laser power also increases linearly with the clock frequency (see Eq. (4)). Overall, the photo-core's power consumption is smaller than the systolic array counterpart up to an array size of 256×256 .

3) Power Efficiency: Figure 5(c) shows the power efficiency (IPS/W) of electronic systolic arrays and photo-cores for

different array sizes and frequencies. We observe that, for the photo-core, 128×128 is the most power-efficient array size for all three networks and all four clock frequencies. The power efficiency of the photo-core increases up to an array size of 128×128 because the laser power does not dominate the power consumption when the array size is small. Beyond a certain size, the laser power increases significantly and dominates the power consumption of the photo-core. Additionally, increasing the array size results in an increase in the throughput provided the utilization of the photo-core is high. However, here too, beyond a certain array size, the utilization decreases and so the throughput saturates. Therefore, due to the exponentially increasing power and saturating throughput, we observe a drop in the power efficiency beyond an array size of 128×128 .

For systolic arrays, the power increases quadratically with the array dimension m . However, because the throughput increases less than quadratically with larger array dimension, the power efficiency decreases as the array size increases. We observe that photo-core can provide up to **9.87** \times , **9.32** \times , and **7.69** \times better power efficiency for ResNet-50, BERT-large, and RNN-T, respectively, when only GEMM operations are considered.

B. ADEPT: Pipelining GEMM and Non-GEMM Operations

As discussed in Section V-A, the GEMM and non-GEMM operations can be pipelined to increase the throughput of ADEPT. Figure 6 shows the impact of pipelining non-GEMM operations on the inference time of ADEPT when running ResNet-50, BERT-large and RNN-T. For ResNet-50, we compute the max-pool, average-pool, ReLU activations and softmax layers in the digital electronic ASIC. In BERT-large, we perform the layer norm, GELU and softmax operations in the digital electronic ASIC. In RNN-T, we execute the element-wise addition and multiplication, sigmoid, and tanh operations (within an LSTM layer) on the digital electronic ASIC. Although the non-GEMM operations comprise a small percentage of the networks' operations, they can lead to a large overhead if not pipelined carefully. When pipelined, the non-GEMM operations and the GEMM operations can be performed in parallel.

In Figure 6, we can see that ResNet-50 has the least amount of overhead due to non-GEMM operations. With batch normalizations folded, ReLU becomes the most frequent non-GEMM operation, which can be effectively overlapped with the GEMM operations. The division and exponential operations in GELU, softmax, sigmoid, and tanh within BERT-large and RNN-T increase the number of cycles spent in the digital electronic ASIC. As batch size increases, GEMM operations are performed more efficiently because more input vectors are multiplied with the same tile—weights are reused more frequently. On the other hand, the cycles spent on non-GEMM operations increase linearly with batch size. Effectively, we observe a larger increase in the time spent on the non-GEMM operations than the increase in time spent on the GEMM operations with increasing batch size. As a

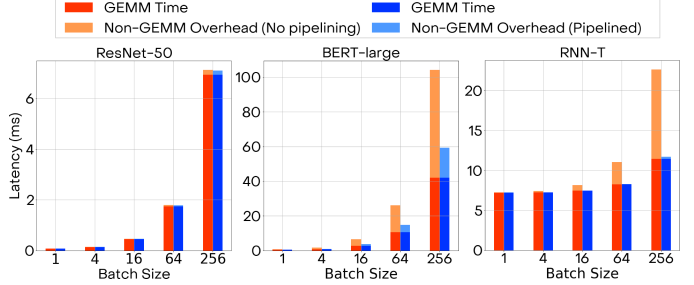


Fig. 6: *Impact of pipelining non-GEMM operations with GEMM operations in ADEPT with a 128×128 photo-core operating at 10 GHz clock frequency. We report the latency of evaluating one batch of inputs for three networks in a non-pipelined (red) and pipelined (blue) manner. The results are calculated for different batch sizes.*

result, a smaller portion of the non-GEMM operations can be overlapped with the GEMM operations. We observe a reduction in latency of up to **5.73%** in ResNet-50, **43.03%** in BERT-large, and **48.22%** in RNN-T when we pipeline the non-GEMM and GEMM operations.

C. ADEPT: Maximizing the Batch Size with Optimized Buffering

Up until now, we used a large batch size of 256 to evaluate the saturated throughput of both ADEPT and systolic arrays. However, given that the SRAM arrays have limited sizes, an inference with batch size of 256 may not fit within the activation SRAM. Frequent DRAM accesses, which are significantly slower than SRAM accesses, can significantly hurt the performance of the system.

For this analysis, we choose an activation SRAM of size 100 MB and a weight SRAM of size 300 MB to ensure that the weights of all the three networks can comfortably fit within ADEPT. Figure 7 shows the usage of the activation SRAM array for the current batch and the next batch when using our optimized DRAM access mechanism (See Section V-B) for the three networks. We limit the batch size to the maximum value where inference on the entire batch can be completed without any DRAM transfers (58, 88, and 50 for ResNet-50, BERT-large, and RNN-T, respectively). The activation SRAM stores the inputs and outputs of all GEMM and non-GEMM operations over time. If the GEMM and non-GEMM operations are running at the same time (pipelined), the memory usage includes both of the operations' activation data.

Figure 7 shows that the networks do not use the whole SRAM array throughout the inference. For ResNet-50 and RNN-T, the memory usage is maximum in the early layers of the inference and then the usage decreases. This creates an opportunity to transfer the inputs for the next batch. For BERT-large, the usage is same for 16 identical encoder layers. Therefore, the next batch can only be transferred during the last encoder layer after the usage goes down.

We compare the performance of this optimized buffering technique against double buffering [72]: a common method

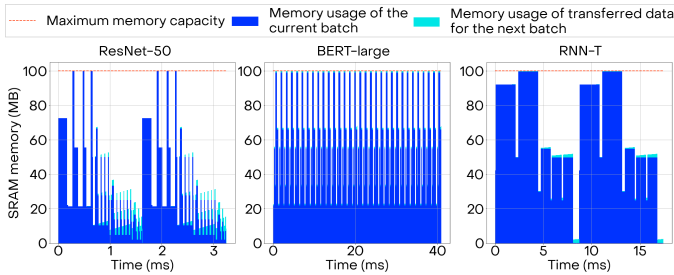


Fig. 7: SRAM usage for computing on the current batch of inputs along with data transfer for the next batch of inputs within ADEPT. Both input and output activations for the current batch must be stored, but only the input activation must be transferred for the next batch. A 128×128 photo-core operating at 10 GHz clock frequency is used with batch sizes of 58, 88, and 50 for ResNet-50, BERT-large, and RNN-T, respectively. The optimized data transfer strategy is considered here with a maximum SRAM capacity of 100 MB.

for minimizing the impact of data transfer latency. In double buffering, one half of the memory is used for the current process (inference) while the other half is used for transferring the inputs for the next process. As a result, the maximum batch sizes of this scheme, for the three networks, are half of those of the optimized buffering scheme. For ResNet-50 and BERT-large, optimized buffering technique increases the throughput only by **1.3%** and **0.4%** compared to double-buffering. This is because the throughputs for these two networks have already saturated for the batch sizes considered. Remarkably, however, optimized data transfer increases the throughput of RNN-T by **89.7%** over double buffering.

D. ADEPT vs. Electronic Systolic Arrays: A System Comparison

In this section, we include all the components and optimizations previously discussed and provide a system-level comparison between ADEPT and an electronic systolic array. The optimizations introduced for ADEPT (Section V) are also applied to the systolic array system. The various components of power consumption in the full ADEPT system are laser power, ADC/DAC power, E-O/O-E conversion power, memory power (SRAM and DRAM), and electronic ASIC power. Similarly for the systolic array system, we look at the power consumption of the systolic array, memory power (SRAM and DRAM), and electronic ASIC power for non-GEMM operations separately. The power and area consumption of a 128×128 ADEPT and a 128×128 OS systolic array are shown in Figure 8. Both systems operate at 10 GHz in the comparison.

The power consumption of the system with systolic array is dominated by the systolic array PEs (more than 90%) while the power consumption of ADEPT is more balanced. ADEPT consumes **$6.35\times$** , **$4.49\times$** and **$11.53\times$** less power, provides **$6.35\times$** , **$4.27\times$** and **$10.96\times$** better power efficiency (IPS/W), and provides **$5.85\times$** , **$3.92\times$** and **$10.08\times$** better power-area efficiency (IPS/W \cdot mm 2) compared to the system with systolic

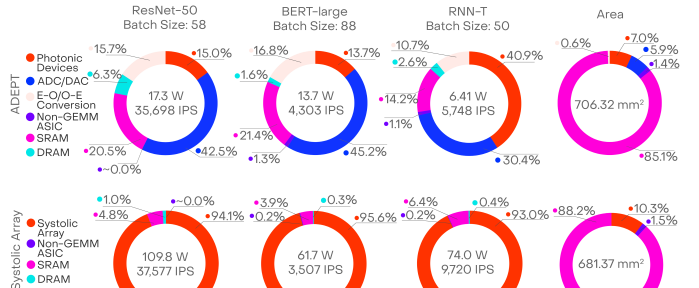


Fig. 8: Average power distribution and area distribution of (top) ADEPT (128×128 , 10 GHz photo-core) and (bottom) the systolic array system (128×128 , 10 GHz array, OS dataflow)

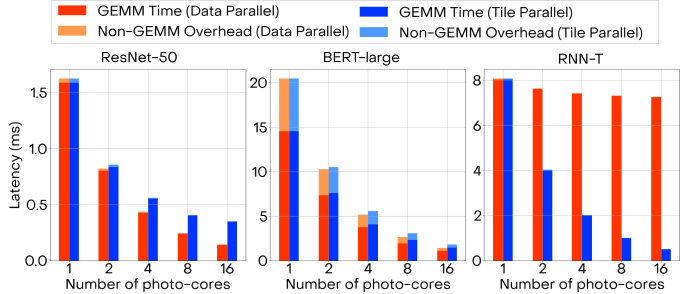


Fig. 9: Latency of ADEPT (128×128 photo-core, operating at 10 GHz clock frequency) when evaluating the three neural networks with different numbers of photo-cores. Two separate parallelization paradigms are considered: data parallelism and tile parallelism..

array for ResNet-50, BERT-large, and RNN-T, respectively. We observe that SRAM dominates the area distribution for both electronic systolic arrays and ADEPT for the chosen configuration.

E. ADEPT: Parallelism

Using multiple photo-cores in ADEPT can further increase the throughput. However, to fully leverage the parallelism in the multi-photo-core architecture, the network needs to be efficiently mapped between multiple photo-cores. Additionally, the number of non-GEMM operation blocks needs to be proportionally increased.

We consider three types of parallelism: data parallelism, tile parallelism, and WDM parallelism (See Section IV-C). Figure 9 shows how the latency scales with increasing number of photo-core counts for both data and tile parallelism. We use the batch sizes previously considered (see Section VII-C), i.e., 58, 88, and 50 for ResNet-50, BERT-large, and RNN-T, respectively. We keep these values constant as we increase the number of photo-cores.

Data parallelism provides an almost linear decrease in inference latency with increasing photo-core count when the number of input vectors within a batch is large enough to be shared among the photo-cores. The latency is dominated by MVM operations for large inputs sizes, and so as the number of photo-cores increases, the throughput proportionally increases. We observe this in ResNet-50 and BERT-large where

the input matrices are large enough to be shared among the photo-cores without significantly reducing the utilization. In contrast, when the number of input vectors per core decreases, the reduction in latency saturates due to the decrease in the utilization of the photo-cores. We observe this in RNN-T. Data parallelism provides **11.30**× lower latency for Resnet-50 and **14.47**× lower latency for BERT-large when we increase the photo-core count from 1 to 16. The reduction in latency for RNN-T is only **1.11**× even when 16 photo-cores are used.

The advantage of tile parallelism is limited by the number of tiles in a GEMM operation. The networks with larger weight matrices (i.e., BERT-large and RNN-T) better exploit this parallelism. Tile parallelism affords **11.24**× and **16.0**× lower latency for BERT-large and RNN-T, respectively, when we increase the photo-core count from 1 to 16. Tile parallelism, however, only reduces the latency of ResNet-50 by **4.62**× when using 16 photo-cores instead of 1.

In both data and tile parallel approaches, the latency of non-GEMM operations decreases almost linearly with the increase in the number of logical units. Most non-GEMM operations are element-wise and do not have dependency between elements within the same input (the only exceptions within the three networks considered are max-pool, average-pool, and softmax).

Multiple photo-cores means a linear increase in the area and the power consumption for the analog photonic computing unit. WDM provides an opportunity to reduce this area usage. WDM allows the input vectors to be mapped across the different wavelengths that are routed to same photo-core. Therefore, WDM offers the same throughput without using multiple copies of the MZI array and weight DACs. When we compare data parallelism with n photo-cores against a single photo-core leveraging n wavelengths in WDM, the photo-core with WDM uses $(n-1)m^2$ fewer MZIs and $(n-1)m^2/\zeta$ fewer weight DACs. As an example, for $n = 4$ wavelengths, on average for ResNet-50, BERT-large, and RNN-T, using WDM results in **1.41**× better power-area efficiency (IPS/W·mm²) compared to using 4 parallel photo-cores in a data parallel manner. This number goes up to **1.53**× for $n = 8$ and **1.87**× for $n = 16$.

VIII. RELATED WORK

A coherent nanophotonics circuit (similar to the one used in ADEPT) designed using programmable photonic arrays was recently proposed to accelerate DNN inference [75]. In this work, they use an MZI array specifically tailored for a 2-layer fully connected neural network which is small compared to the DNNs in today’s AI systems. With today’s large DNNs, the noise accumulation and power loss would grow too much for the accelerator to be feasible. By fixing the MZI array size and using tiling, ADEPT can handle both problems and provide a flexible accelerator design which can be used for different DNNs. Similarly, [14], [30], [95] use very shallow photonic neural networks on MNIST and Fashion MNIST datasets. Although they report promising TOPS results, these numbers do not accurately reflect the real-life performance.

Other previous photonic computing architecture works including DEAP-CNN [8], PCNNA [53], HolyLight [52], Al-bireo [79], PIXEL [80], CrossLight [82], and DNNARA [60] use microring resonators (MRRs) for their multiply and/or accumulate operations. MRRs have the advantage of having a smaller area than MZIs. However, they require thermal stabilization and have lower ER [81]. Hence, using MZIs is a more scalable solution (See Section II). Moreover, all previous works on photonic DNN accelerators are designed specifically for convolution operations, or they report results only for CNNs and only for GEMM operations. While these works can provide some insights for CNNs that have a limited variety of operations, the conclusions in these works are not applicable to the other type of DNN architectures (e.g., transformers, LSTMs, etc.) that contain a wider range of operations. In our work, we provide a complete system analysis which includes non-GEMM operations, memory accesses, and parallelism strategies. Our results show that electro-photonic accelerators can be used for different types of DNNs, and the system can provide significant benefits compared to its electrical counterpart.

IX. DISCUSSION

We build our analysis on the assumption that 8-bit precision is adequate for meeting the accuracy requirements of the three state-of-the-art DNNs we used. If we were to increase the precision, the power consumption of ADCs/DACs would roughly increase as 2^B where B is the number of bits. However, previous works on quantization show that an 8-bit precision is sufficient to maintain the accuracy of state-of-the-art neural networks within 1% of the FP32 accuracy after performing several epochs of quantization-aware retraining [47], [91]. Additionally, MLCommons’ latest inference results (v1.0) for datacenter benchmarks (which include the same DNNs we use for evaluation) are largely submitted with INT8 precision [56].

In our analysis, SRAM dominates the area of both ADEPT and electronic systolic arrays. Ideally, we would like to use large local SRAMs to have large batches. However, SRAM size is limited in a chip-scale system. To increase SRAM cache size, scale-out to multiple accelerators is required. The problem of designing scaled-out systems, mapping a DNN model onto many accelerators, and orchestrating the communication between them is part of our future work.

Lastly, it is important to carefully formulate performance metrics for a DNN accelerator system. In particular, we use IPS as the throughput performance metric instead of TOPS. The TOPS metric fails to consider processing unit utilization which is not likely to be unity. The TOPS metric therefore yields results that are too optimistic, while IPS is a direct indication of actual throughput. In our analysis, we do not set an upper bound on latency as a limitation. Larger batch sizes provide better throughput, although associated latencies may be higher. Latency-bounded throughput is another important metric to consider. In this case, batch size should be limited to meet latency requirements—potentially limiting overall throughput that can be realized.

X. CONCLUSION

In this paper, we proposed an end-to-end hybrid system containing an electro-photonic accelerator called ADEPT for accelerating DNN inference. We showed that ADEPT has a similar throughput performance to the widely-accepted systolic array architecture while consuming significantly less power—avoiding the power wall that currently limits high performance accelerators. We showed that accelerating DNN inference with photonics requires tight interplay between the photonic units for GEMM operations and the electronic logic units for non-GEMM operations. With the introduced optimization methods for pipelining operations and data transfers, we showed that we can leverage the high throughput of the photonics GEMM accelerator without being bottlenecked by electronic units. Overall, we are optimistic that photonic computing is nigh, and we are looking forward to the application of the technology in real-life. Given the performance advantage (in terms of IPS/W or IPS/W·mm²), we are confident that the technology will find its rightful place within the Cambrian explosion of AI accelerators.

ACKNOWLEDGEMENT

We would like to thank Saumil Bandyopadhyay (MIT), Ryan Hamerly (MIT), Alexander Sludds (MIT), Leila Delshadtehrani (BU) and Zahra Azad (BU) for the valuable discussions and their insightful suggestions.

REFERENCES

- [1] “Genus Synthesis Solution.” [Online]. Available: https://www.cadence.com/en_US/home/tools/digital-design-and-signoff/synthesis/genus-synthesis-solution.html
- [2] “GF22nm FD-SOI Technology,” <https://globalfoundries.com/sites/default/files/product-briefs/pb-22fdx-26-web.pdf>.
- [3] “Large-scale Silicon Photonic Switches with Movable Directional Couplers,” *Optica*, vol. 2, no. 4, pp. 370–375, Apr 2015. [Online]. Available: <http://www.osapublishing.org/optica/abstract.cfm?URI=optica-2-4-370>
- [4] S. Akiyama, T. Baba, M. Imai, T. Akagawa, M. Takahashi, N. Hirayama, H. Takahashi, Y. Noguchi, H. Okayama, T. Horikawa, and T. Usuki, “12.5-Gb/s operation with 0.29-V·cm V π L using silicon Mach-Zehnder modulator based-on forward-biased pin diode,” *Opt. Express*, vol. 20, no. 3, pp. 2911–2923, Jan 2012. [Online]. Available: <http://www.opticsexpress.org/abstract.cfm?URI=oe-20-3-2911>
- [5] D. Amodei, “AI and Compute,” Sep 2020. [Online]. Available: <https://openai.com/blog/ai-and-compute/>
- [6] A. Anderson, A. Vasudevan, C. Keane, and D. Gregg, “Low-memory GEMM-based Convolution Algorithms for Deep Neural Networks,” 2017. [Online]. Available: [arXiv:1709.03395](https://arxiv.org/abs/1709.03395)
- [7] S. Bandyopadhyay, R. Hamerly, and D. Englund, “Hardware Error Correction for Programmable Photonics,” *arXiv*, vol. abs/2103.04993, 2021. [Online]. Available: <https://arxiv.org/abs/2103.04993>
- [8] V. Bangari, B. A. Marquez, H. Miller, A. N. Tait, M. A. Nahmias, T. F. de Lima, H.-T. Peng, P. R. Prucnal, and B. J. Shastri, “Digital Electronics and Analog Photonics for Convolutional Neural Networks (DEAP-CNNs),” *IEEE Journal of Selected Topics in Quantum Electronics*, vol. 26, no. 1, pp. 1–13, 2020.
- [9] Q. Bao, H. Zhang, Z. Ni, Y. Wang, L. Polavarapu, Z. Shen, Q.-H. Xu, D. Tang, and K. P. Loh, “Monolayer Graphene as a Saturable Absorber in a Mode-locked Laser,” *Nano Research*, vol. 4, no. 3, pp. 297–307, 2011. [Online]. Available: <https://doi.org/10.1007/s12274-010-0082-9>
- [10] T. E. Bell, “Optical Computing: A Field in Flux,” *IEEE Spectrum*, vol. 23, no. 8, pp. 34–38, 1986.
- [11] L. Bernstein, A. Sludds, R. Hamerly, V. Sze, J. Emer, and D. Englund, “Freely Scalable and Reconfigurable Optical Hardware for Deep Learning,” *Scientific Reports*, vol. 11, no. 1, p. 3144, 2021. [Online]. Available: <https://doi.org/10.1038/s41598-021-82543-3>
- [12] W. Bogaerts, P. De Heyn, T. Van Vaerenbergh, K. De Vos, S. Kumar Selvaraja, T. Claes, P. Dumon, P. Bienstman, D. Van Thourhout, and R. Baets, “Silicon Microring Resonators,” *Laser & Photonics Reviews*, vol. 6, no. 1, pp. 47–73, 2012. [Online]. Available: <https://onlinelibrary.wiley.com/doi/abs/10.1002/lpor.201100017>
- [13] T. B. Brown, B. Mann, N. Ryder, M. Subbiah, J. Kaplan, P. Dhariwal, A. Neelakantan, P. Shyam, G. Sastry, A. Askell, S. Agarwal, A. Herbert-Voss, G. Krueger, T. Henighan, R. Child, A. Ramesh, D. M. Ziegler, J. Wu, C. Winter, C. Hesse, M. Chen, E. Sigler, M. Litwin, S. Gray, B. Chess, J. Clark, C. Berner, S. McCandlish, A. Radford, I. Sutskever, and D. Amodei, “Language Models Are Few-shot Learners,” 2020.
- [14] D. Brunner and P. Demetri, “Competitive Photonic Neural Networks,” *Nature Photonics*, vol. 15, pp. 323–324, 2021. [Online]. Available: <https://doi.org/10.1038/s41566-021-00803-0>
- [15] H. J. Caulfield, “Parallel N4 Weighted Optical Interconnections,” *Appl. Opt.*, vol. 26, no. 19, pp. 4039–4040, Oct 1987. [Online]. Available: <http://ao.osa.org/abstract.cfm?URI=ao-26-19-4039>
- [16] L. Cavigelli and L. Benini, “Origami: A 803-GOp/s/W Convolutional Network Accelerator,” *IEEE Transactions on Circuits and Systems for Video Technology*, vol. 27, no. 11, pp. 2461–2475, 2017.
- [17] T. Chen, Z. Du, N. Sun, J. Wang, C. Wu, Y. Chen, and O. Temam, “DianNao: A Small-Footprint High-Throughput Accelerator for Ubiquitous Machine-Learning,” *SIGARCH Comput. Archit. News*, vol. 42, no. 1, p. 269–284, Feb. 2014. [Online]. Available: <https://doi.org/10.1145/2654822.2541967>
- [18] Y. Chen, T. Krishna, J. S. Emer, and V. Sze, “Eyeriss: An Energy-Efficient Reconfigurable Accelerator for Deep Convolutional Neural Networks,” *IEEE Journal of Solid-State Circuits*, vol. 52, no. 1, pp. 127–138, 2017.
- [19] Y. Chen, T. Luo, S. Liu, S. Zhang, L. He, J. Wang, L. Li, T. Chen, Z. Xu, N. Sun, and O. Temam, “DaDianNao: A Machine-Learning Supercomputer,” in *2014 47th Annual IEEE/ACM International Symposium on Microarchitecture*, 2014, pp. 609–622.
- [20] Y. Chen, Y. Xie, L. Song, F. Chen, and T. Tang, “A Survey of Accelerator Architectures for Deep Neural Networks,” *Engineering*, vol. 6, no. 3, pp. 264–274, 2020. [Online]. Available: <https://www.sciencedirect.com/science/article/pii/S2095809919306356>
- [21] Z. Chen, J. Wang, H. He, and X. Huang, “A Fast Deep Learning System Using GPU,” in *2014 IEEE International Symposium on Circuits and Systems (ISCAS)*, 2014, pp. 1552–1555.
- [22] S. Chetlur, C. Woolley, P. Vandermersch, J. Cohen, J. Tran, B. Catanzaro, and E. Shelhamer, “cuDNN: Efficient Primitives for Deep Learning,” *CoRR*, vol. abs/1410.0759, 2014. [Online]. Available: <http://arxiv.org/abs/1410.0759>
- [23] J. Choquette, W. Gandhi, O. Giroux, N. Stam, and R. Krashinsky, “Nvidia a100 tensor core gpu: Performance and innovation,” *IEEE Micro*, vol. 41, no. 2, pp. 29–35, 2021.
- [24] W. R. Clements, P. C. Humphreys, B. J. Metcalf, W. S. Kolthammer, and I. A. Walmsley, “Optimal Design for Universal Multiport Interferometers,” *Optica*, vol. 3, no. 12, pp. 1460–1465, Dec 2016. [Online]. Available: <http://www.osapublishing.org/optica/abstract.cfm?URI=optica-3-12-1460>
- [25] H. Cui, H. Zhang, G. R. Ganger, P. B. Gibbons, and E. P. Xing, “Geeps: Scalable deep learning on distributed gpus with a gpu-specialized parameter server,” in *Proceedings of the Eleventh European Conference on Computer Systems*, ser. EuroSys ’16. New York, NY, USA: Association for Computing Machinery, 2016. [Online]. Available: <https://doi.org/10.1145/2901318.2901323>
- [26] J. Devlin, M.-W. Chang, K. Lee, and K. Toutanova, “BERT: Pre-training of Deep Bidirectional Transformers for Language Understanding,” 2019. [Online]. Available: [arXiv:1810.04805](https://arxiv.org/abs/1810.04805)
- [27] Z. Du, R. Fasthuber, T. Chen, P. Ienne, L. Li, T. Luo, X. Feng, Y. Chen, and O. Temam, “ShiDianNao: Shifting Vision Processing Closer to the Sensor,” in *2015 ACM/IEEE 42nd Annual International Symposium on Computer Architecture (ISCA)*, 2015, pp. 92–104.
- [28] C. Farabet, B. Martini, B. Corda, P. Akselrod, E. Culurciello, and Y. LeCun, “NeuFlow: A Runtime Reconfigurable Dataflow Processor for Vision,” in *CVPR 2011 WORKSHOPS*, 2011, pp. 109–116.
- [29] C. Farabet, Y. Lecun, K. Kavukcuoglu, B. Martini, P. Akselrod, S. Talay, and E. Culurciello, *Large-Scale FPGA-Based Convolutional Networks*. Cambridge University Press, 2011, p. 399–419.
- [30] J. Feldmann, N. Youngblood, M. Karpov, H. Gehring, X. Li, M. Stappers, M. Le Gallo, X. Fu, A. Lukashchuk, A. S. Raja, J. Liu, C. D. Wright, A. Sebastian, T. J. Kippenberg, W. H. Pernice, and

H. Bhaskaran, "Parallel Convolutional Processing Using an Integrated Photonic Tensor Core," *Nature*, vol. 589, no. 7840, pp. 52–58, 2021. [Online]. Available: <https://doi.org/10.1038/s41586-020-03070-1>

[31] K. Giewont, K. Nummy, F. A. Anderson, J. Ayala, T. Barwicz, Y. Bian, K. K. Dezfulian, D. M. Gill, T. Houghton, S. Hu, B. Peng, M. Rakowski, S. Rauch, J. C. Rosenberg, A. Sahin, I. Stobert, and A. Stricker, "300-mm Monolithic Silicon Photonics Foundry Technology," *IEEE Journal of Selected Topics in Quantum Electronics*, vol. 25, no. 5, pp. 1–11, 2019.

[32] M. Guo, J. Mao, S.-W. Sin, H. Wei, and R. P. Martins, "A 5 GS/s 29 mW Interleaved SAR ADC With 48.5 dB SNDR Using Digital-Mixing Background Timing-Skew Calibration for Direct Sampling Applications," *IEEE Access*, vol. 8, pp. 138 944–138 954, 2020.

[33] R. Hamerly, S. Bandyopadhyay, and D. Englund, "Accurate Self-Configuration of Rectangular Multiport Interferometers," *arXiv*, vol. abs/2106.03249, 2021. [Online]. Available: <https://arxiv.org/abs/2106.03249>

[34] R. Hamerly, S. Bandyopadhyay, and D. Englund, "Stability of Self-Configuring Large Multiport Interferometers," *arXiv*, vol. abs/2106.04363, 2021. [Online]. Available: <https://arxiv.org/abs/2106.04363>

[35] N. C. Harris, J. Carolan, D. Bunandar, M. Prabhu, M. Hochberg, T. Baehr-Jones, M. L. Fanto, A. M. Smith, C. C. Tison, P. M. Alsing, and D. Englund, "Linear Programmable Nanophotonic Processors," *Optica*, vol. 5, no. 12, pp. 1623–1631, Dec 2018. [Online]. Available: <http://www.osapublishing.org/optica/abstract.cfm?URI=optica-5-12-1623>

[36] N. C. Harris, Y. Ma, J. Mower, T. Baehr-Jones, D. Englund, M. Hochberg, and C. Galland, "Efficient, Compact and Low Loss Thermo-optic Phase Shifter in Silicon," *Opt. Express*, vol. 22, no. 9, pp. 10 487–10 493, May 2014. [Online]. Available: <http://www.opticsexpress.org/abstract.cfm?URI=oe-22-9-10487>

[37] K. He, X. Zhang, S. Ren, and J. Sun, "Deep Residual Learning for Image Recognition," in *2016 IEEE Conference on Computer Vision and Pattern Recognition (CVPR)*, 2016, pp. 770–778.

[38] Y. He, T. N. Sainath, R. Prabhavalkar, I. McGraw, R. Alvarez, D. Zhao, D. Rybach, A. Kannan, Y. Wu, R. Pang, Q. Liang, D. Bhatia, Y. Shangguan, B. Li, G. Pundak, K. C. Sim, T. Bagby, S. yin Chang, K. Rao, and A. Gruenstein, "Streaming End-to-end Speech Recognition For Mobile Devices," 2018. [Online]. Available: [arXiv:1811.06621](https://arxiv.org/abs/1811.06621)

[39] M. Horowitz, "Computing's Energy Problem (and What We Can Do About It)," in *2014 IEEE International Solid-State Circuits Conference Digest of Technical Papers (ISSCC)*, 2014, pp. 10–14.

[40] K. Hsu, D. Brady, and D. Psaltis, "Experimental Demonstrations of Optical Neural Computers," in *Neural Information Processing Systems*, D. Anderson, Ed. American Institute of Physics, 1988. [Online]. Available: <https://proceedings.neurips.cc/paper/1987/file/8f14e45fceea167a5a36dedd4bea2543-Paper.pdf>

[41] H.-Y. Huang, X.-Y. Chen, and T.-H. Kuo, "A 10-GS/s NRZ/Mixing DAC With Switching-Glitch Compensation Achieving SFDR gt; 64/50 dBc Over the First/Second Nyquist Zone," *IEEE Journal of Solid-State Circuits*, pp. 1–1, 2021.

[42] Huimin Li, Xitian Fan, Li Jiao, Wei Cao, Xuegong Zhou, and Lingli Wang, "A High Performance FPGA-based Accelerator for Large-scale Convolutional Neural Networks," in *2016 26th International Conference on Field Programmable Logic and Applications (FPL)*, 2016, pp. 1–9.

[43] L. N. Huynh, Y. Lee, and R. K. Balan, "Deepmon: Mobile gpu-based deep learning framework for continuous vision applications," in *Proceedings of the 15th Annual International Conference on Mobile Systems, Applications, and Services*, ser. MobiSys '17. New York, NY, USA: Association for Computing Machinery, 2017, p. 82–95. [Online]. Available: <https://doi.org/10.1145/3081333.3081360>

[44] J. D. Jackson, *Classical Electrodynamics*. New York, NY: Wiley, 1975. [Online]. Available: <https://cds.cern.ch/record/100964>

[45] B. Jacob, S. Kligys, B. Chen, M. Zhu, M. Tang, A. Howard, H. Adam, and D. Kalenichenko, "Quantization and Training of Neural Networks for Efficient Integer-Arithmetic-Only Inference," 2017. [Online]. Available: [arXiv:1712.05877](https://arxiv.org/abs/1712.05877)

[46] N. P. Jouppi, C. Young, N. Patil, D. Patterson, G. Agrawal, R. Bajwa, S. Bates, S. Bhatia, N. Boden, A. Borchers, R. Boyle, P.-I. Cantin, C. Chao, C. Clark, J. Coriell, M. Daley, M. Dau, J. Dean, B. Gelb, T. V. Ghaemmaghami, R. Gottipati, W. Gulland, R. Hagmann, C. R. Ho, D. Hogberg, J. Hu, R. Hundt, D. Hurt, J. Ibarz, A. Jaffey, A. Jaworski, A. Kaplan, H. Khaitan, D. Killebrew, A. Koch, N. Kumar, S. Lacy, J. Laudon, J. Law, D. Le, C. Leary, Z. Liu, K. Lucke, A. Lundin, G. MacKean, A. Maggiore, M. Mahony, K. Miller, R. Nagarajan, R. Narayanaswami, R. Ni, K. Nix, T. Norrie, M. Omernick, N. Penukonda, A. Phelps, J. Ross, M. Ross, A. Salek, E. Samadiani, C. Severn, G. Sizikov, M. Snelham, J. Souter, D. Steinberg, A. Swing, M. Tan, G. Thorson, B. Tian, H. Toma, E. Tuttle, V. Vasudevan, R. Walter, W. Wang, E. Wilcox, and D. H. Yoon, "In-datacenter performance analysis of a tensor processing unit," in *Proceedings of the 44th Annual International Symposium on Computer Architecture*, ser. ISCA '17. New York, NY, USA: Association for Computing Machinery, 2017, p. 1–12. [Online]. Available: <https://doi.org/10.1145/3079856.3080246>

[47] R. Krishnamoorthi, "Quantizing deep convolutional networks for efficient inference: A whitepaper," *CoRR*, vol. abs/1806.08342, 2018. [Online]. Available: <http://arxiv.org/abs/1806.08342>

[48] Y. LeCun and C. Cortes, "MNIST Handwritten Digit Database." [Online]. Available: <http://yann.lecun.com/exdb/mnist/>

[49] X. Li and L. Zhou, "A survey of high-speed high-resolution current steering DACs," *Journal of Semiconductors*, vol. 41, no. 20060024, p. 111404, Oct 2020. [Online]. Available: <http://www.jos.ac.cn/article/id/47363c32-84f1-4705-a902-2d07194df2b8>

[50] S. Lischke, D. Knoll, C. Mai, L. Zimmermann, A. Peczek, M. Kroh, A. Trusch, E. Krune, K. Voigt, and A. Mai, "High Bandwidth, High Responsivity Waveguide-coupled Germanium p-i-n Photodiode," *Opt. Express*, vol. 23, no. 21, pp. 27 213–27 220, Oct 2015. [Online]. Available: <http://www.opticsexpress.org/abstract.cfm?URI=oe-23-21-27213>

[51] W. Liu, D. Anguelov, D. Erhan, C. Szegedy, S. Reed, C.-Y. Fu, and A. C. Berg, "SSD: Single Shot MultiBox Detector," in *Computer Vision – ECCV 2016*, B. Leibe, J. Matas, N. Sebe, and M. Welling, Eds. Cham: Springer International Publishing, 2016, pp. 21–37.

[52] W. Liu, W. Liu, Y. Ye, Q. Lou, Y. Xie, and L. Jiang, "HolyLight: A Nanophotonic Accelerator for Deep Learning in Data Centers," in *2019 Design, Automation Test in Europe Conference Exhibition (DATE)*, 2019, pp. 1483–1488.

[53] A. Mehrabian, Y. Al-Kabani, V. J. Sorger, and T. El-Ghazawi, "PCNNA: A Photonic Convolutional Neural Network Accelerator," in *2018 31st IEEE International System-on-Chip Conference (SOCC)*, Sep 2018. [Online]. Available: <http://dx.doi.org/10.1109/SOCC.2018.8618542>

[54] D. A. B. Miller, "Self-configuring Universal Linear Optical Component," *Photon. Res.*, vol. 1, no. 1, pp. 1–15, Jun 2013. [Online]. Available: <http://www.osapublishing.org/prj/abstract.cfm?URI=prj-1-1-1>

[55] M. Mischuglio, A. Mehrabian, Z. Hu, S. I. Azzam, J. George, A. V. Kildishev, M. Pelton, and V. J. Sorger, "All-optical Nonlinear Activation Function for Photonic Neural Networks," *Opt. Mater. Express*, vol. 8, no. 12, pp. 3851–3863, Dec 2018. [Online]. Available: <http://www.osapublishing.org/ome/abstract.cfm?URI=ome-8-12-3851>

[56] MLCommons, "Datacenter v1.0 results." [Online]. Available: <https://mlcommons.org/en/inference-datacenter-10/>

[57] G. Mourou, B. Brocklesby, T. Tajima, and J. Limpert, "The future is fibre accelerators," *Nature Photonics*, vol. 7, no. 4, pp. 258–261, 2013. [Online]. Available: <https://doi.org/10.1038/nphoton.2013.75>

[58] V. Panayotov, G. Chen, D. Povey, and S. Khudanpur, "Librispeech: An ASR Corpus Based on Public Domain Audio Books," in *2015 IEEE International Conference on Acoustics, Speech and Signal Processing (ICASSP)*, 2015, pp. 5206–5210.

[59] A. Parashar, M. Rhu, A. Mukkara, A. Puglielli, R. Venkatesan, B. Khailany, J. Emer, S. W. Keckler, and W. J. Dally, "SCNN: An Accelerator for Compressed-sparse Convolutional Neural Networks," in *2017 ACM/IEEE 44th Annual International Symposium on Computer Architecture (ISCA)*, 2017, pp. 27–40.

[60] J. Peng, Y. Alkabani, S. Sun, V. J. Sorger, and T. El-Ghazawi, "DNNARA: A Deep Neural Network Accelerator Using Residue Arithmetic and Integrated Photonics," in *49th International Conference on Parallel Processing - ICPP*, ser. ICPP '20. New York, NY, USA: Association for Computing Machinery, 2020. [Online]. Available: <https://doi.org/10.1145/3404397.3404467>

[61] M. Poot and H. X. Tang, "Broadband Nanoelectromechanical Phase Shifting of Light on a Chip," *Applied Physics Letters*, vol. 104, no. 6, p. 061101, 2014. [Online]. Available: <https://doi.org/10.1063/1.4864257>

[62] A. Radford and K. Narasimhan, "Improving Language Understanding by Generative Pre-Training," 2018. [Online]. Available: <https://paperswithcode.com/paper/improving-language-understanding-by>

[63] A. Radford, J. Wu, R. Child, D. Luan, D. Amodei, and I. Sutskever, "Language Models are Unsupervised Multitask Learners,"

2019. [Online]. Available: <https://paperswithcode.com/paper/language-models-are-unsupervised-multitask>

[64] P. Rajpurkar, J. Zhang, K. Lopyrev, and P. Liang, "SQuAD: 100,000+ questions for machine comprehension of text," in *Proceedings of the 2016 Conference on Empirical Methods in Natural Language Processing*. Austin, Texas: Association for Computational Linguistics, Nov. 2016, pp. 2383–2392. [Online]. Available: <https://aclanthology.org/D16-1264>

[65] M. Reck, A. Zeilinger, H. J. Bernstein, and P. Bertani, "Experimental Realization of Any Discrete Unitary Operator," *Phys. Rev. Lett.*, vol. 73, pp. 58–61, Jul 1994. [Online]. Available: <https://link.aps.org/doi/10.1103/PhysRevLett.73.58>

[66] V. J. Reddi, C. Cheng, D. Kanter, P. Mattson, G. Schmuelling, C. Wu, B. Anderson, M. Breughe, M. Charlebois, W. Chou, R. Chukka, C. Coleman, S. Davis, P. Deng, G. Diamos, J. Duke, D. Fick, J. S. Gardner, I. Hubara, S. Idgunji, T. B. Jablin, J. Jiao, T. S. John, P. Kanwar, D. Lee, J. Liao, A. Lokhmotov, F. Massa, P. Meng, P. Micikevicius, C. Osborne, G. Pekhimenko, A. T. R. Rajan, D. Sequeira, A. Sirasao, F. Sun, H. Tang, M. Thomson, F. Wei, E. Wu, L. Xu, K. Yamada, B. Yu, G. Yuan, A. Zhong, P. Zhang, and Y. Zhou, "MLPerf Inference Benchmark," in *2020 ACM/IEEE 47th Annual International Symposium on Computer Architecture (ISCA)*, 2020, pp. 446–459.

[67] O. A. Reimann and W. F. Kosonocky, "Progress in Optical Computer Research," *IEEE Spectrum*, vol. 2, no. 3, pp. 181 – 195, 1965.

[68] G. Roelkens, J. Van Campenhout, J. Brouckaert, D. Van Thourhout, R. Baets, P. R. Romeo, P. Regreny, A. Kazmierczak, C. Seassal, X. Letartre, G. Hollinger, J. Fedeli, L. Di Cioccio, and C. Lagahe-Blanchard, "III-V/Si Photonics by Die-to-wafer Bonding," *Materials Today*, vol. 10, no. 7, pp. 36–43, 2007. [Online]. Available: <https://www.sciencedirect.com/science/article/pii/S1369702107701785>

[69] O. Ronneberger, P. Fischer, and T. Brox, "U-NET: Convolutional Networks for Biomedical Image Segmentation," in *Medical Image Computing and Computer-Assisted Intervention – MICCAI 2015*, N. Navab, J. Hornegger, W. M. Wells, and A. F. Frangi, Eds. Cham: Springer International Publishing, 2015, pp. 234–241.

[70] O. Russakovsky, J. Deng, H. Su, J. Krause, S. Satheesh, S. Ma, Z. Huang, A. Karpathy, A. Khosla, M. Bernstein, A. C. Berg, and L. Fei-Fei, "ImageNet Large Scale Visual Recognition Challenge," *International Journal of Computer Vision (IJCV)*, vol. 115, no. 3, pp. 211–252, 2015.

[71] A. Samajdar, Y. Zhu, P. N. Whatmough, M. Mattina, and T. Krishna, "SCALE-Sim: Systolic CNN Accelerator," *arXiv*, vol. abs/1811.02883, 2018. [Online]. Available: <http://arxiv.org/abs/1811.02883>

[72] J. C. Sancho and D. J. Kerbyson, "Analysis of double buffering on two different multicore architectures: Quad-core Opteron and the Cell-BE," in *2008 IEEE International Symposium on Parallel and Distributed Processing*, 2008, pp. 1–12.

[73] M. Sankaradas, V. Jakkula, S. Cadambi, S. Chakradhar, I. Durdanovic, E. Cosatto, and H. P. Graf, "A Massively Parallel Coprocessor for Convolutional Neural Networks," in *2009 20th IEEE International Conference on Application-specific Systems, Architectures and Processors*, 2009, pp. 53–60.

[74] B. J. Shastri, A. N. Tait, T. Ferreira de Lima, W. H. P. Pernice, H. Bhaskaran, C. D. Wright, and P. R. Prucnal, "Photonics for Artificial Intelligence and Neuromorphic Computing," *Nature Photonics*, vol. 15, no. 2, pp. 102–114, 2021. [Online]. Available: <https://doi.org/10.1038/s41566-020-00754-y>

[75] Y. Shen, N. C. Harris, S. Skirlo, M. Prabhu, T. Baehr-Jones, M. Hochberg, X. Sun, S. Zhao, H. Larochelle, D. Englund, and M. Soljačić, "Deep Learning with Coherent Nanophotonic Circuits," *Nature Photonics*, vol. 11, no. 7, pp. 441–446, 2017. [Online]. Available: <https://doi.org/10.1038/nphoton.2017.93>

[76] Shen, Yun, Wang, Xiaodong, Zhang, Wei, Qiu, Ciyan, and Cheng, Xiulan, "Fabrication of Depletion Type Micro-ring Modulator with High Extinction Ratio and High Coupling Quality Factor," *MATEC Web Conf.*, vol. 139, p. 00066, 2017. [Online]. Available: <https://doi.org/10.1051/matecconf/201713900066>

[77] B. Shi, N. Calabretta, D. Bunandar, D. Englund, and R. Stabile, "WDM Weighted Sum in an 8x8 SOA-Based InP Cross-Connect for Photonic Deep Neural Networks," in *2018 Photonics in Switching and Computing (PSC)*, 2018, pp. 1–3.

[78] B. Shi, N. Calabretta, and R. Stabile, "Deep Neural Network Through an InP SOA-Based Photonic Integrated Cross-Connect," *IEEE Journal of Selected Topics in Quantum Electronics*, vol. 26, no. 1, pp. 1–11, 2020.

[79] K. Shiflett, A. Karanth, R. Bunescu, and A. Louri, "Albireo: Energy-Efficient Acceleration of Convolutional Neural Networks via Silicon Photonics," in *2021 ACM/IEEE 48th Annual International Symposium on Computer Architecture (ISCA)*, 2021.

[80] K. Shiflett, D. Wright, A. Karanth, and A. Louri, "PIXEL: Photonic Neural Network Accelerator," in *2020 IEEE International Symposium on High Performance Computer Architecture (HPCA)*, 2020, pp. 474–487.

[81] C. Sun, M. Wade, Y. Lee, J. Orcutt, L. Alloatti, M. Georgas, A. Waterman, J. Shainline, R. Avizienis, S. Lin, B. Moss, R. Kumar, F. Pavanello, A. Atabaki, H. Cook, A. J. Ou, J. Leu, Y. hsin Chen, K. Asanović, R. J. Ram, M. Popovic, and V. Stojanović, "Single-chip microprocessor that communicates directly using light," *Nature*, vol. 528, pp. 534–538, 2015.

[82] F. Sunny, A. Mirza, M. Nikdast, and S. Pasricha, "Crosslight: A cross-layer optimized silicon photonic neural network accelerator," *arXiv*, vol. abs/2102.06960, 2021. [Online]. Available: <https://arxiv.org/abs/2102.06960>

[83] A. N. Tait, T. Ferreira de Lima, M. A. Nahmias, H. B. Miller, H.-T. Peng, B. J. Shastri, and P. R. Prucnal, "Silicon Photonic Modulator Neuron," *Phys. Rev. Applied*, vol. 11, p. 064043, Jun 2019. [Online]. Available: <https://link.aps.org/doi/10.1103/PhysRevApplied.11.064043>

[84] E. Timurdogan, C. V. Poulton, M. J. Byrd, and M. R. Watts, "Electric Field-induced Second-order Nonlinear Optical Effects in Silicon Waveguides," *Nature Photonics*, vol. 11, no. 3, pp. 200–206, 2017. [Online]. Available: <https://doi.org/10.1038/nphoton.2017.14>

[85] X. Tu, C. Song, T. Huang, Z. Chen, and H. Fu, "State of the art and perspectives on silicon photonic switches," *Micromachines*, vol. 10, no. 1, 2019. [Online]. Available: <https://www.mdpi.com/2072-666X/10/1/51>

[86] A. Van den Bosch, M. Steyaert, and W. Sansen, *Solving Static and Dynamic Performance Limitations for High Speed D/A Converters*. Boston, MA: Springer US, 2002, pp. 189–210. [Online]. Available: https://doi.org/10.1007/0-306-47950-8_10

[87] M. R. Watts, J. Sun, C. DeRose, D. C. Trotter, R. W. Young, and G. N. Nielson, "Adiabatic Thermo-optic Mach-Zehnder Switch," *Opt. Lett.*, vol. 38, no. 5, pp. 733–735, Mar 2013. [Online]. Available: <http://ol.osa.org/abstract.cfm?URI=ol-38-5-733>

[88] G. Wetzstein, A. Ozcan, S. Gigan, S. Fan, D. Englund, M. Soljačić, C. Denz, D. A. B. Miller, and D. Psaltis, "Inference in artificial intelligence with deep optics and photonics," *Nature*, vol. 588, no. 7836, pp. 39–47, 2020. [Online]. Available: <https://doi.org/10.1038/s41586-020-2973-6>

[89] C. M. Wilkes, X. Qiang, J. Wang, R. Santagati, S. Paesani, X. Zhou, D. A. B. Miller, G. D. Marshall, M. G. Thompson, and J. L. O'Brien, "60dB High-extinction Auto-configured Mach-Zehnder Interferometer," *Opt. Lett.*, vol. 41, no. 22, pp. 5318–5321, Nov 2016. [Online]. Available: <http://ol.osa.org/abstract.cfm?URI=ol-41-22-5318>

[90] C. Wu, H. Yu, S. Lee, R. Peng, I. Takeuchi, and M. Li, "Programmable phase-change metasurfaces on waveguides for multimode photonic convolutional neural network," *Nature Communications*, vol. 12, no. 1, p. 96, 2021. [Online]. Available: <https://doi.org/10.1038/s41467-020-20365-z>

[91] H. Wu, P. Judd, X. Zhang, M. Isaev, and P. Micikevicius, "Integer quantization for deep learning inference: Principles and empirical evaluation," *CoRR*, vol. abs/2004.09602, 2020. [Online]. Available: <https://arxiv.org/abs/2004.09602>

[92] Y. Wu, M. Schuster, Z. Chen, Q. V. Le, M. Norouzi, W. Macherey, M. Krikun, Y. Cao, Q. Gao, K. Macherey, J. Klingner, A. Shah, M. Johnson, X. Liu, Łukasz Kaiser, S. Gouws, Y. Kato, T. Kudo, H. Kazawa, K. Stevens, G. Kurian, N. Patil, W. Wang, C. Young, J. Smith, J. Riesa, A. Rudnick, O. Vinyals, G. Corrado, M. Hughes, and J. Dean, "Google's Neural Machine Translation System: Bridging the Gap between Human and Machine Translation," *arXiv*, vol. abs/1609.08144, 2016. [Online]. Available: <https://arxiv.org/abs/1609.08144>

[93] H. Xiao, K. Rasul, and R. Vollgraf, "Fashion-MNIST: A Novel Image Dataset for Benchmarking Machine Learning Algorithms," *arXiv*, vol. abs/1708.07747, 2017. [Online]. Available: <http://arxiv.org/abs/1708.07747>

[94] H. Xu and Y. Shi, "Flat-top cwdm (de)multiplexer based on mzi with bent directional couplers," *IEEE Photonics Technology Letters*, vol. 30, no. 2, pp. 169–172, 2018.

- [95] X. Xu, M. Tan, B. Corcoran, J. Wu, A. Boes, T. G. Nguyen, S. T. Chu, B. E. Little, D. G. Hicks, R. Morandotti, A. Mitchell, and D. J. Moss, “11 TOPS Photonic Convolutional Accelerator for Optical Neural Networks,” *Nature*, vol. 589, no. 7840, pp. 44–51, 2021. [Online]. Available: <https://doi.org/10.1038/s41586-020-03063-0>
- [96] A. Yazdanbakhsh, K. Samadi, N. S. Kim, and H. Esmaeilzadeh, “GANAX: A Unified MIMD-SIMD Acceleration for Generative Adversarial Networks,” in *Proceedings of the 45th Annual International Symposium on Computer Architecture*, ser. ISCA ’18. IEEE Press, 2018, p. 650–661. [Online]. Available: <https://doi.org/10.1109/ISCA.2018.00060>
- [97] C. Zhang, P. Li, G. Sun, Y. Guan, B. Xiao, and J. Cong, “Optimizing FPGA-Based Accelerator Design for Deep Convolutional Neural Networks,” in *Proceedings of the 2015 ACM/SIGDA International Symposium on Field-Programmable Gate Arrays*, ser. FPGA ’15. New York, NY, USA: Association for Computing Machinery, 2015, p. 161–170. [Online]. Available: <https://doi.org/10.1145/2684746.2689060>
- [98] Y. Zuo, B. Li, Y. Zhao, Y. Jiang, Y.-C. Chen, P. Chen, G.-B. Jo, J. Liu, and S. Du, “All-optical Neural Network with Nonlinear Activation Functions,” *Optica*, vol. 6, no. 9, pp. 1132–1137, Sep 2019. [Online]. Available: <http://www.osapublishing.org/optica/abstract.cfm?URI=optica-6-9-1132>